Three-dimensional structure and multistable optical switching of triple-twisted particle-like excitations in anisotropic fluids

Ivan I. Smalyukh[1,2,3]*, Yves Lansac[2,4], Noel A. Clark[1,2] and Rahul P. Trivedi[1,2]

Control of structures in soft materials with long-range order forms the basis for applications such as displays, liquid-crystal biosensors, tunable lenses, distributed feedback lasers, muscle-like actuators and beam-steering devices. Bistable, tristable and multistable switching of well-defined structures of molecular alignment is of special interest for all of these applications. Here we describe the facile optical creation and multistable switching of localized configurations in the molecular orientation field of a chiral nematic anisotropic fluid. These localized chiro-elastic particle-like excitations—dubbed 'triple-twist torons'— are generated by vortex laser beams and embed the localized three-dimensional (3D) twist into a uniform background. Confocal polarizing microscopy and computer simulations reveal their equilibrium internal structures, manifesting both skyrmion-like and Hopf fibration features. Robust generation of torons at predetermined locations combined with both optical and electrical reversible switching can lead to new ways of multistable structuring of complex photonic architectures in soft materials.

L iquid crystals combine properties of crystalline solids and isotropic fluids in many unique and unexpected ways, giving rise to an increasingly broad range of technological[1–9] and biomedical[1,10–12] applications. Nematic liquid crystals of rod-shaped molecules are classic anisotropic fluids characterized by long-range orientational ordering and a ground state with a spatially uniform molecular long-axis orientation $\hat{n}(\mathbf{r})$ called the 'director'[13,14]. Introduction of molecular chirality leads to chiral nematic liquid-crystal (CNLC) phases having more exotic ground states. In the cholesteric phase, the ground-state director field $\hat{n}(\mathbf{r})$ shows a spatial twist, precessing at a constant rate along a 'helical axis' line. Blue phases consist of lattices of packed 'double-twist cylinders', in which $\hat{n}(\mathbf{r})$ is parallel to the cylinder axis at its centre and shows two-dimensional (2D) radial twist to form a barber-pole-like pattern on the cylinder surface[13,15]. Cholesteric-phase and blue-phase ground-state structures can be suppressed by applied fields or by treated surfaces that couple to $\hat{n}(\mathbf{r})$, rendering the CNLC uniform and thus frustrated with respect to its preference for twist. This frustration, however, can be relieved locally, and we report here several particle-like excitations in $\hat{n}(\mathbf{r})$, dubbed triple-twist torons (T3s), enabling the reappearance of twist in a CNLC initially rendered uniform. By focusing Laguerre–Gaussian (LG) vortex beams[16,17], T3s are optically generated at will at a selected place and then structurally characterized with full detail in 3D. The basic T3 configuration is a double-twist cylinder closed on itself in the form of a torus (Fig. 1a) and coupled to the surrounding uniform field by point or line topological singularities (Fig. 1b–f). Remarkably, the torons enable twist in all three spatial dimensions and are stabilized by strong energy barriers associated with nucleation of topological defects. We show that T3 structure and stability can be accounted for by the basic field theory of elastic $\hat{n}(\mathbf{r})$ deformations and use computer simulations

to obtain the equilibrium field and elastic energy that closely match experimental findings.

In our experiments, the CNLC of equilibrium helical pitch p (distance over which the director rotates by 2π) is confined into a cell of thickness d with the inner surfaces of glass plates treated to align CNLC molecules along the normal to the plates, $\hat{z}$ (ref. 18). These boundary conditions are incompatible with the ground-state cholesteric-phase and blue-phase twist, and tend to unwind twisted structures forcing uniform bulk alignment with $\hat{n}(\mathbf{r}) \| \hat{z}$ (refs 18, 19). The helical structure is unwound (nematic-like) when the cell gap is much smaller than the pitch ($p \gg d$), whereas for larger cell gaps ($p \ll d$), the director twists freely in the centre of the sample and meets the vertical-boundary conditions at the glass plates by introducing splay and bend distortions of $\hat{n}(\mathbf{r})$ (ref. 19). The CNLC unwinding in the studied cells occurs at $d/p \approx 1$ or smaller, at which we first assure that the sample with a uniform initial $\hat{n}(\mathbf{r}) \| \hat{z}$ is free of the so-called cholesteric fingers[18,19] and then optically induce the localized T3 structures. To generate the torons, we use Laguerre–Gaussian vortex beams that belong to a family of beams with helical phase fronts and phase singularities. The helical phase fronts of the Laguerre–Gaussian beam of charge l comprise l intertwined helical surfaces forming an optical screw dislocation along the beam axis. The integer charge value $|l|$ defines the number of twists the phase of the light makes in one wavelength and the sign of l defines the twist direction[16,17]. Laguerre–Gaussian beams with such optical screw dislocations are known to carry an orbital angular momentum of $l\hbar$ per photon[20] and have attracted a great deal of recent interest in imaging, laser manipulation and optical communications[16,17,21,22]. Although liquid-crystal spatial light modulators[21] and even droplets of liquid crystals[22] have been used to generate these optical vortices, the laser-induced realignment effects of Laguerre–Gaussian beams in liquid-crystalline phases of different symmetries and the ensuing
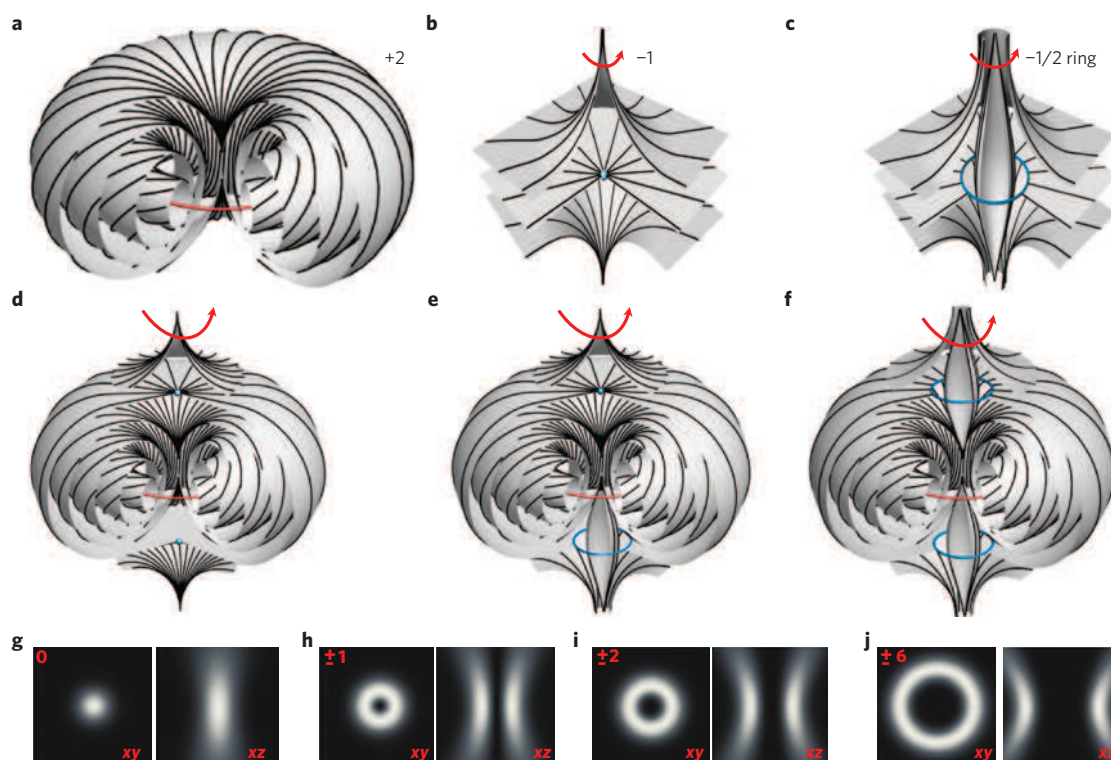
139

Figure 1 | T3 field configurations generated by Laguerre–Gaussian beams and embedded into a uniform field by defects. a, Toron structure with the topological charge '+2' owing to the twist-escaped non-singular disclination ring of strength $s = +1$ shown by the red line. **b,c**, '−1' hyperbolic point defect (**b**) and a ring of $s = -1/2$ disclination topologically equivalent to a '−1' point defect (**c**), both showing twist of $\hat{n}(\mathbf{r})$ with the sense of twist shown by the red arrows. **d**, T3-1 configuration with the toron accompanied by two hyperbolic point defects. **e**, T3-2 structure containing a point defect and a disclination ring. **f**, T3-3 configuration with two $s = -1/2$ defect rings. **g-j**, Light-intensity distributions in the lateral xy (left) and axial xz (right) planes of the Laguerre–Gaussian beams of topological charge marked for each of the image pairs; the square cross-sections are 4 μm wide.

structures remain to be explored. The CNLCs studied here have helicoidal ground-state director structure and are of special interest from this standpoint. In our experiments, the beams of charge $l = 0 - \pm 10$ and intensity distributions in the lateral and axial planes shown in Fig. 1g–j are focused into the bulk of an unwound CNLC with the vertical $\hat{n}(\mathbf{r})$ along the beam's axis and typical $d/p = 0.75$–1.1. When the laser power is increased above a threshold value $P_{th} = (30$–50) mW, the beam rotates $\hat{n}(\mathbf{r})$ towards the lateral $\mathbf{E}(\mathbf{r}) \perp \hat{z}$, inducing a distortion, owing to the positive dielectric anisotropy of the CNLC for the light's electric field $\mathbf{E}(\mathbf{r})$. This initial distortion (birefringent spot observed in polarizing microscopy) disappears within 5–10 ms after turning off the laser to minimize the elastic energy[13]. However, if the laser power is increased above the second threshold $P > (1.2$–2.2)P_{th}, this distortion transforms into one of the T3 structures persisting even after the laser is switched off (Fig. 2). The generated T3s are embedded in a sea of uniform $\hat{n}(\mathbf{r}) \| \hat{z}$ and have a characteristic size $\approx p$ in all directions. Three-dimensional images and cross-sections obtained by fluorescence confocal polarizing microscopy[23] (FCPM) for different linear and circular FCPM polarizations, such as those shown in Fig. 3 and Supplementary Figs S1 and S2, allow reconstruction of $\hat{n}(\mathbf{r})$ for the three distinct types of T3 observed (Fig. 1d–f).

The structure that emerges is the toron shown in Fig. 1a, a double-twist cylinder looped on itself around the $\hat{z}$ axis. In the toroid's midplane, the structure is skyrmion-like[24] as the director at the centre is vertical and twists by 180° in outward radial directions matching the vertical $\hat{n}(\mathbf{r})$ in the far field around the structure. The $\hat{n}(\mathbf{r})$ is tangent to the circular axis of the toroid and rotates in all directions when moving away from it (Figs 1 and 3b). The uniformly twisted field lines of $\hat{n}(\mathbf{r})$ on a family of nested tori resemble the stereographic projection of the Hopf

fibration[25–27], while being localized in a finite volume of space because of the presence of defects embedding the toron into a uniform field. Mapping the director field at the toroid surfaces into the order parameter space of the CNLC covers the sphere twice[14] and implies that the topological charge of the toron structure is +2, suggesting that defects of opposite charge are needed to embed it into the uniform field[14,28]. Indeed, FCPM imaging (Fig. 3 and Supplementary Figs S1 and S2) reveals that the orientational order within the localized T3 structures is locally broken on topological defect points (Fig. 1b) or ring-shaped lines (Fig. 1c), depending on the type of T3 structure formed. The line defects (also known as disclinations) are classified by their strength s defined as a number of revolutions by 2π that $\hat{n}(\mathbf{r})$ makes around the defect core when one circumnavigates this core once. CNLC disclinations are often observed 'escaping in the third dimension' through twist to form non-singular structure with $\hat{n}(\mathbf{r})$ in their core along the defect line[18]. The toron contains a 'twist-escaped' $s = +1$ disclination ring shown by the red line in Fig. 1a (the $s = +1$ defect ring is equivalent to a +2 point defect; ref. 14). The director field $\hat{n}(\mathbf{r})$ of the toron is matched to the surrounding uniform alignment by introducing defects of total charge '−2' such as the '−1' hyperbolic point defects (Fig. 1b) or $s = -1/2$ disclination rings (Fig. 1c). Different defect-proliferated torons are induced next to each other as shown in Fig. 2a: T3-1 with two hyperbolic −1 point defects shown by the blue dots in Fig. 1d, T3-3s with two $s = -1/2$ disclination rings shown by the blue lines in Fig. 1f and T3-2s with combinations of line and point defects such as the one in Fig. 1e. As the $s = -1/2$ disclination rings are equivalent to '−1' point defects[14], topological charge of T3s in the uniform field is always conserved. Remarkably, the defects do not annihilate as commonly observed[13,14], but rather are stably unbound to enable the 3D twist
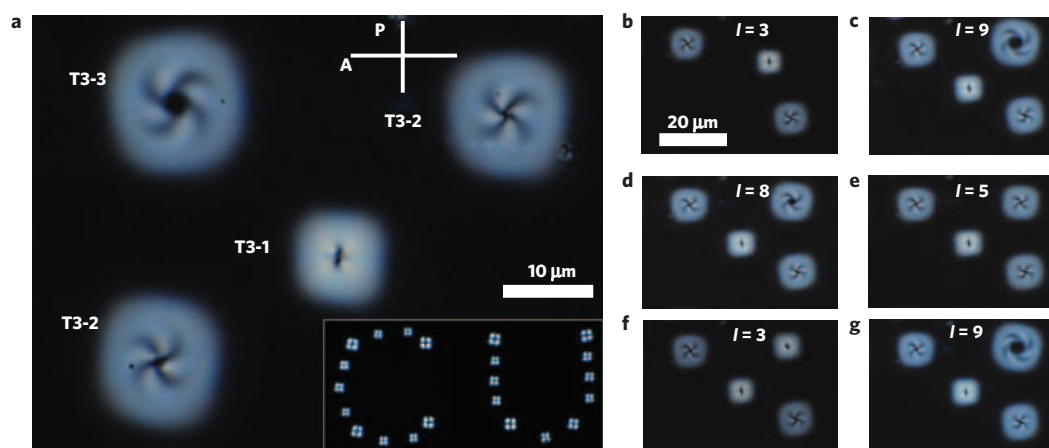
Figure 2 | Predetermined optical generation and switching of the toron structures. a, Polarizing optical microscopy texture showing T3-1 (the smallest), two T3-2s of opposite winding (intermediate size) and T3-3 (the largest structure) generated next to each other. The inset shows the letters 'CU' obtained by optical generation of four T3-2s per letter at the letters' vertices and T3-1 elsewhere within the characters. The orientations of the crossed polarizer (P) and analyser (A) are shown by the white bars. **b**, Polarizing microscopy image showing that the two T3-2s of opposite spiralling and the T3-1 can be generated at an arbitrary location in the sample and then moved to the desired position (such as the one shown in **c**) using optical manipulation by laterally shifting the generating infrared laser beam. **c**, After optically moving the T3-1 to the image centre, the new T3-3 structure is generated in the top right corner of the image. **d**–**g**, This T3-3 structure is shown transforming into a T3-2 structure (**d,e**), then to T3-1 (**f**) and again to the T3-3 configuration (**g**) by using Laguerre–Gaussian beams of appropriate topological charge values l marked on the images. Note that the T3-3 structures in **c,d,g** have different diameters of the disclination rings at the top and bottom surfaces and all T3-2s and T3-3s have lateral dimensions 1.1–1.5 times larger than T3-1s.
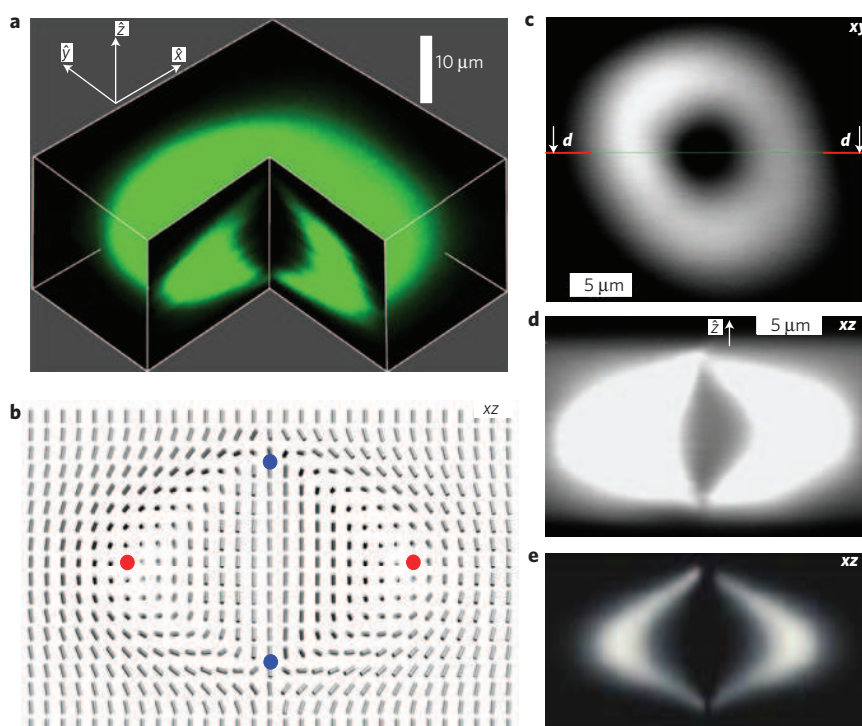

Figure 3 | FCPM imaging and computer simulations of laser-generated torons. a, Three-dimensional image of the T3-1 configuration obtained using FCPM with circularly polarized probing light. **b**, Vertical cross-section of the $\hat{n}(\mathbf{r})$ of the corresponding 3D T3-1 structure obtained by numerical minimization of the elastic free energy; the blue circles denote the hyperbolic point defects and the red circles show the twist-escaped disclination intersecting the plane of the cross-section. **c**, In-plane FCPM cross-section passing through the central plane of the T3 structure and containing the circular axis of the torus; the red bars indicate the location of the vertical cross-section. **d,e**, Experimental vertical FCPM cross-section (**d**) and the corresponding computer-simulated FCPM texture (**e**) obtained for circularly polarized probing light and the equilibrium director field shown in **b**. The confinement ratio is $d/p = 1$ in both the experiments and the simulations.

of $\hat{n}(\mathbf{r})$. The 3D FCPM images and vertical cross-sections allow us to visualize and distinguish structural details of different T3s (Fig. 3 and Supplementary Figs S1 and S2). For example, FCPM textures in Supplementary Fig. S2 not only identify the imaged optically

generated structures as T3-2s, but also show the location of point and ring defects at the top or bottom glass plates.

By varying l of the generating vortex beams, we can selectively create (Fig. 2a) and switch (Fig. 2b–g) the toron configurations. For

Table 1 | Material parameters of the used nematic hosts and chiral additives.

Material/property	K_{11} (pN)	K_{22} (pN)	K_{33} (pN)	$\Delta\varepsilon_{lf}$	Δn	H_{HTP} of CB-15 (μm^{-1})	H_{HTP} of S-811 (μm^{-1})
MLC-6609	17.2	7.51	17.9	−3.7	0.078	-	−10.5
ZLI-3412	14.1	6.7	15.5	+3.4	0.078	+6.3	−8.8
MLC-6815	-	-	-	+8.1	0.052	+6.5	−10.7

example, the letters 'CU' in the inset of Fig. 2a are composed of T3-2s at the corners and T3-1s elsewhere within the characters. Generation of different T3s depends on the initial laser-induced director tilt from the vertical alignment, which, in turn, depends on the intensity distributions shown in Fig. 1g–j. Beams having large $|l|$ with high-intensity lobes in the axial plane pointing outward from the low-intensity centre generate T3-2s or T3-3s, whereas the beams with small $|l|$ generate T3-1s. For example, in a cell with $p \approx d = 5\,\mu m$, the T3-1 structure is induced by the Laguerre–Gaussian beams of $l = \pm(0-4)$, the T3-2 is observed for $l = \pm(4-8)$ and T3-3 is observed for $|l| > 8$. Therefore, T3s can be reversibly transformed between each other as shown in the top right corner of Fig. 2c–g. The threshold generating laser powers are comparable for all T3s and vary from 60 mW for $l = 0$ to 110 mW for $l = 10$. Generating threshold power increases with increasing cell thickness and helical pitch (70 mW for the $l = 0$ beam and a cell of $p \approx d \approx 15\,\mu m$) but is independent of the sign of l and the CNLC handedness. T3s can be switched between each other or transformed into a uniform unwound state by applying electric fields; however, the spontaneous transformation between these structures requires nucleation of more defects defining energy barriers much larger than the thermal energy[13]. Consequently, all three torons and the unwound state can be realized next to each other (Fig. 2). By varying cell thickness and pitch, we have generated T3s of size $\sim p$ ranging from $\sim$500 nm to $\sim$200 μm that were stable at $d/p \sim 1$ and showing $\hat{n}(\mathbf{r})$ structures with no explicit dependence on d or p individually. We have used materials with both positive and negative low-frequency dielectric anisotropy $\Delta\varepsilon_{lf}$ (Table 1). For positive $\Delta\varepsilon_{lf}$ (nematic hosts ZLI-3412 and MLC-6815 doped with the chiral agent CB-15), we have observed that the T3s can be transformed into a uniform nematic-like state by applying a voltage of $\sim$10 V at 1 kHz to the transparent electrodes of the cell. In CNLCs with negative dielectric anisotropy (MLC-6609 doped with the chiral agent S-811), the low-frequency electric field tends to reorient $\hat{n}(\mathbf{r})$ perpendicular to the electric field lines and reduces the threshold laser power of the Laguerre–Gaussian beam needed to generate T3s because the action of the electric field augments that of the optical field. The T3s and their periodic arrays or other structural arrangements are stable over a long time at no external fields, but can also be 'erased' by applying a voltage pulse to transparent electrodes or 'reshaped' by a laser beam. For example, the structure in the inset of Fig. 2a can be electrically erased in $\sim$5 ms (typical response of a CNLC cell of thickness $\sim$5 μm; ref. 13) and optically reshaped into a structure such as that shown in Fig. 2g in less than a second.

Detailed information about the equilibrium $\hat{n}(\mathbf{r})$ and energy of T3-1 is obtained from computer simulations by minimizing the Frank elastic energy of the CNLC (ref. 13):

$$F_{\text{elastic}} = \int \left\{ \frac{K_{11}}{2}(\nabla \cdot \hat{n})^2 + \frac{K_{22}}{2}\left[\hat{n} \cdot (\nabla \times \hat{n}) + \frac{2\pi}{p}\right]^2 \right.$$
$$+ \frac{K_{33}}{2}[\hat{n} \times (\nabla \times \hat{n})]^2 - K_{24}[\nabla \cdot [\hat{n}(\nabla \cdot \hat{n})$$
$$\left. + \hat{n} \times (\nabla \times \hat{n})]] \right\} dV \qquad (1)$$

where K_{11}, K_{22}, K_{33} and K_{24} are elastic constants describing splay, twist, bend and saddle-splay deformations, respectively. To mimic the experiments, F_{elastic} is supplemented with a term that describes coupling to the electric field $\mathbf{E}_{LG}$ of the generating Laguerre–Gaussian beam, $F_{\text{field}} = -((\varepsilon_0\Delta\varepsilon)/2)\int(\mathbf{E}_{LG} \cdot \hat{n})^2 dV$, where $\Delta\varepsilon = n_e^2 - n_o^2$ is the dielectric anisotropy and n_e and n_o are the extraordinary and ordinary refractive indices at the optical frequency of the generating beam, respectively. The equilibrium $\hat{n}(\mathbf{r})$ is first obtained by minimizing $F_{\text{elastic}} + F_{\text{field}}$ in the presence of $\mathbf{E}_{LG}$ and then further equilibrated when the laser is turned off. Minimization is carried out through the so-called 'director relaxation method'[29] on 3D discrete grids using a finite-difference scheme (see Supplementary Information). Using the obtained minimum-energy $\hat{n}(\mathbf{r})$ in different cross-sections of the structure, we computer-simulate the corresponding FCPM textures of the T3-1 structure using a standard simulation procedure[30]. The details of the T3 structure at $d/p = 1$ are further explored by comparing the full 3D computer-simulated $\hat{n}(\mathbf{r})$ with the experimental results (Fig. 3 and Supplementary Figs S1–S3). For example, in the vertical cross-section of the T3-1 director configuration (Fig. 3b) similar to the case of experimentally reconstructed structure (Fig. 1d), one sees two point defects near the top and bottom plates as well as the twist of $\hat{n}(\mathbf{r})$ in both radial and axial directions. The calculated pattern of FCPM signal intensity $I_{FCPM}(\mathbf{r})$ shown in Fig. 3e closely matches the experimental image (Fig. 3d). Similar comparative analysis is carried out for other cross-sections of the T3-1 structure, such as the vertical and in-plane cross-sections containing the point defects at the top and bottom glass plates and the central plane of T3-1 with the double-twisted $\hat{n}(\mathbf{r})$ (Fig. 3 and Supplementary Figs S1 and S3). For example, both the experimental and the simulated cross-section planes crossing point defects parallel to the top and bottom glass plates shown in Supplementary Fig. S1 reveal that the spiralling of $\hat{n}(\mathbf{r})$ near the point defects is in opposite directions at the top and bottom plates. The calculated equilibrium $\hat{n}(\mathbf{r})$ and respective $I_{FCPM}(\mathbf{r})$ consistently match the experimental ones.

Elastic-energy-density plots for the equilibrated T3-1 structure show that the unwound $\hat{n}(\mathbf{r})$ surrounding the toron has minimum contributions of the splay and bend terms in equation (1) but large twist energy (Fig. 4a–c). T3s locally minimize the twist and saddle-splay terms of F_{elastic} (Fig. 4c,d) at the expense of enhancing the splay and bend distortions (Fig. 4a,b) and introducing defect cores. Similarly to the case of blue phases[13], the saddle-splay term in equation (1) gives a negative contribution lowering the energy of torons (Fig. 4d), although T3-1s can be stabilized even for $K_{24} = 0$. Consequently, the triple-twist region has low elastic energy and the regions around the hyperbolic point defects have high energy, as shown by iso-energy surfaces in Fig. 4e. For $d \approx p$, contributions of terms in equation (1) are such that T3s have elastic energy comparable to that of the unwound state (Supplementary Fig. S4), but are separated by elastic-energy barriers that are large compared with thermal energy. The topological skeleton[31,32] built from the simulated field (Fig. 4f) consists of two hyperbolic point defects near the top and bottom surfaces and a twist-escaped disclination ring. In Fig. 4f, the skeleton is shown along with the streamlets tangent to $\hat{n}(\mathbf{r})$, originating close
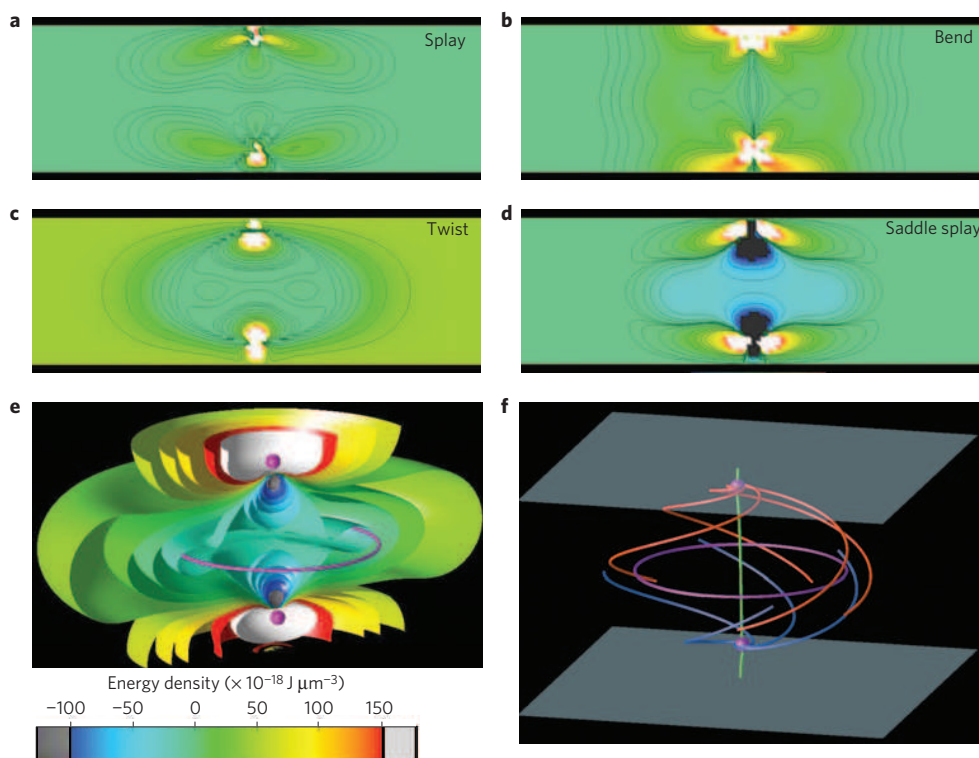
Figure 4 | Elasticity and topology of the T3-1 structure. a–d, Elastic free energy plotted separately for splay (**a**), bend (**b**), twist (**c**) and saddle splay (**d**) distortions within the T3-1 structure and in its vicinity with the surrounding $\hat{n}(\mathbf{r}) \parallel \hat{z}$. **e,** Total elastic energy density isosurfaces showing twisted regions of low free-energy density and also energetically costly regions of defects and strong bend and splay distortions. **f,** Topological skeleton of $\hat{n}(\mathbf{r})$ showing hyperbolic point defects in the vicinity of the top and bottom surfaces (shown by magenta spheres) as well as the twist-escaped $s = +1$ disclination in the midplane coinciding with the circular toroid's axis (magenta line); streamlets tangent to $\hat{n}(\mathbf{r})$ are shown by the red and blue lines for eigendirections perpendicular to $\hat{z}$ and by the green lines for the eigendirection along $\hat{z}$. The colour-coded scale is for the elastic energy density in **a–e**.

to the defects and showing that the $\hat{n}(\mathbf{r})$-spiralling at the top and bottom defects is in opposite directions, consistent with the experiments (Supplementary Fig. S1). A more detailed description of the experimental and numerical studies and the topological analysis of $\hat{n}(\mathbf{r})$ in T3-1s as well as that of T3-2s and T3-3s will be reported elsewhere.

A wide variety of condensed-phase phenomena arise as a result of the existence of particle-like excitations of continuous fields[14]. Out of the three T3s observed in CNLCs with nonpolar symmetry and the S^2/Z_2 order parameter space, one (T3-1) can potentially be realized in polar condensed-matter systems such as chiral magnets with the S^2 order parameter space (Fig. 5); this is in contrast to the T3-2s and T3-3s containing half-integer disclinations that cannot exist in a vector field. Therefore, in addition to their generation in frustrated chiral nematic systems, torons can give origin to new forms of structural self-assembly in other chiral condensed-matter phases, having a role of 'building blocks' similar to that of double-twist cylinders in blue phases[14,15]. The detailed knowledge of their structure may provide the basis for studies of complex twisted fields in condensed matter[24–27] and impinge on the understanding of particle-like excitations in other branches of science.

The minimum size of the optically induced torons is not limited by the wavelength of the generating light and is comparable to the cholesteric pitch p (Supplementary Fig. S4). When the cholesteric pitch is smaller than the wavelength of the generating light, by gradually tuning the laser power just above the toron generation threshold, only one T3 structure can be induced at the centre of the beam. This diffraction-unlimited nature of the process allows optical generation of torons down to ∼100 nm in size even when an infrared laser beam is used. As arbitrary periodic configurations of T3s can be generated for toron sizes
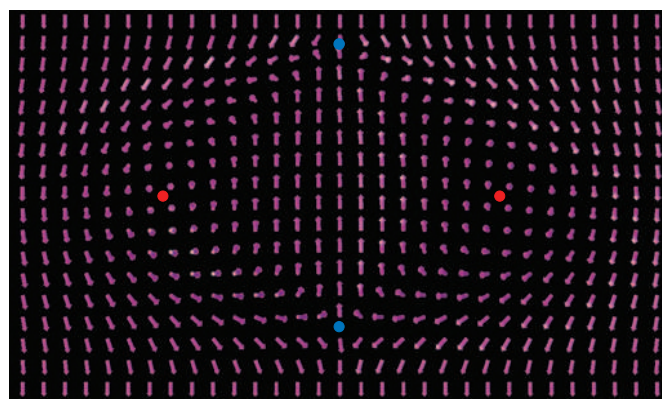

Figure 5 | Vector-field representation of the T3-1 configuration in the axial cross-section. The T3-1 particle-like structure can be realized in fields with polar symmetry and the S^2 order parameter space. The blue circles show the hyperbolic point defects and the red circles show the twist-escaped disclination intersecting the cross-section.

and lattice periodicities ranging from ∼100 nm to 100 μm or larger, potential applications include data-storage devices, light- or voltage-controlled diffraction gratings and all-optical information displays. Both optical and electrical multistable switching of T3s with low-intensity beams or low-voltage electric fields is especially attractive for these applications, as it enables low power consumption and diversifies modes of operation for the ensuing technologies and devices. Although the values of optical anisotropy of thermotropic liquid crystals are typically smaller than 0.5, the refractive index contrast can be enhanced

by doping them with nanoparticles[33,34], potentially enabling photonic-crystal applications. Furthermore, the elasticity-mediated interactions between particles embedded in the liquid-crystal host[35–37] make it interesting, from both fundamental and applied standpoints, to explore how the presence of torons in the host medium translates into the oriented self-organization of immersed inclusions depending on their shape, size and chemical composition or surface treatment[38]. As CNLCs with the T3s assembled into various structures can be photo-polymerized or polymer-stabilized[39,40], the spectrum of potential applications may extend to polymer-stabilized diffraction gratings, flexible displays, electronic books, non-mechanical beam-steering devices and so on.

Robust optical generation of multistable triple-twisted toron structures demonstrates that optical phase singularities in laser beams can allow for the control of topological singularities in materials. It is of special interest to further explore how linked and knotted optical wave dislocations[41–43] could generate topological defects and structures in soft matter as well as how arrays and nodes of liquid-crystal defects, in return, could allow for devising of unusual light beams by controlling their optical phase singularities[41–43]. Torons and their arrays with tunable periodicity and interactions may be used as model systems for probing many-body interactions and condensed-matter phenomena, similarly to the present use of colloids[35–37,44]. The detailed 3D structure of torons reported here may provide new insights into the toroidal DNA condensation[45,46] and DNA arrangement in chromosomes[47]. Furthermore, facile generation and switching of torons open up the possibilities for applications ranging from all-optical devices to new multistable information displays.

Methods

Integrated structure generation and imaging set-up. We have constructed a holographic optical liquid-crystal alignment system (HOLCAS) allowing us to generate focused Gaussian and Laguerre–Gaussian laser beams with controlled polarization states. HOLCAS consists of a liquid-crystal spatial light modulator (LCSLM, from Boulder Nonlinear Systems; ref. 48) and a continuous-wave ytterbium-doped fibre laser (1,064 nm, from IPG Photonics) with an output beam diameter of 5.0 mm. This beam is first expanded to overfill the active area of the LCSLM and then reduced to the size of the back aperture of the microscope objective. This is achieved using two telescopes in the optical train, one before and another after the LCSLM. The reflective electrically addressed phase-only LCSLM with 512×512 pixels ($15 \times 15\,\mu m^2$ each) controls the phase of the incoming beam within $0–2\pi$ radians on a pixel-by-pixel basis at a 30 Hz refresh rate. This modulated light is imaged at the back aperture of the microscope objective acting as a Fourier transform lens. The HOLCAS allows us to produce Gaussian and Laguerre–Gaussian vortex beams of different topological charge l and intensity distributions shown in Fig. 1g–j. The generating beam of typical power within $P = 0–200$ mW is focused into a volume of $\sim 1\,\mu m^3$ at different sample depths and moved in 3D along computer-programmed trajectories[48]. In addition to optical fields, low-frequency electric fields (1 kHz, up to 20 V) were applied using a DS345 generator (Stanford Research Systems) and a Model 7602 wide-band amplifier (Krohn–Hite).

The HOLCAS is integrated with the FCPM (ref. 23) based on the FV300 confocal system with an inverted microscope base IX81 (Olympus). A dichroic mirror (Chroma) is mounted in a rotating filter turret positioned below the microscope objective. The 1,064 nm laser beam is reflected by this dichroic mirror into the objective lens, whereas the visible light (488 nm Ar-laser excitation beam and the fluorescent light from the dye-doped sample) is transmitted through it to/from the confocal microscopy scanning and detection unit. We use $\times 60$ and $\times 100$ oil-immersion objectives with a numerical aperture of 1.4 (60–70% transmission at 1,064 nm) to generate T3s using HOLCAS and to image them using FCPM and polarizing optical microscopy.

We reconstruct $\hat{n}(\mathbf{r})$ using FCPM cross-sections obtained for circular and different linear polarizations as well as using polarizing microscopy textures. For volume rendering of the 3D FCPM images, we use the FV1000 software (Olympus). The FCPM signal intensity scales as $I_{FCPM}(\mathbf{r}) \propto \cos^4\beta$, where β is the angle between the emission/absorption transition dipoles of the dye (both orienting along $\hat{n}(\mathbf{r})$) and the linear FCPM polarization. Confocal cross-sections and 3D images obtained for circularly polarized excitation allow one to determine the tilt of $\hat{n}(\mathbf{r})$ with respect to the cell normal, whereas the complementary images obtained for linearly polarized FCPM probing light reveal the coordinate-dependent $\hat{n}(\mathbf{r})$ (ref. 23). Small excitation laser powers $\ll 1$ mW assure that a laser beam scanned through the sample for imaging purposes does not alter $\hat{n}(\mathbf{r})$ of T3s.

Materials and sample preparation. The cells were assembled using glass plates having transparent indium tin oxide electrodes. To produce strong vertical boundary conditions at the inner surfaces of the plates, we spin-coated thin layers of polyimide JALS-204 (obtained from JSR), which were then cross-linked by baking at $\approx 220\,^{\circ}$C for 1 h. The cell gap thickness was set using either glass spacers uniformly distributed within the cell (one spacer per $\sim 0.5\,mm^2$ area) or strips of mylar film placed along the cell edges. The cell gap thickness was varied within $0.5–200\,\mu m$ and measured after cell assembly using the interference method with a spectrophotometer or laser reflections in a confocal microscope. Series of cells with uniform thickness as well as wedge-shaped cells with varying thickness were filled with materials of different pitch p. The CNLC was introduced into cells by capillary forces when heated to its isotropic phase (to avoid the effects of flow on the alignment). CNLCs are prepared using nematics MLC-6815, ZLI-3412 with positive and MLC-6609 with negative dielectric anisotropy (EM industries). Elastic constants K_{11}, K_{22} and K_{33}, dielectric anisotropy $\Delta\varepsilon_{lf}$ at 1 kHz and optical anisotropy $\Delta n = n_e - n_o$ for the used materials are provided in Table 1. To obtain CNLCs of different handedness, the nematic host is doped with a right-handed chiral additive CB-15 or left-handed S-811 (both from EM Industries). The cholesteric pitch is varied within $p = 1–150\,\mu m$ by adding different concentrations $C_{agent} = 1/(H_{HTP} \times p)$ of the chiral agent (up to 10 wt%). The helical twisting powers H_{HTP} of chiral additives in studied nematic hosts have been determined using the Grandjean–Cano method[18] (Table 1). For the FCPM studies, CNLCs are doped with dye N,N'-bis(2,5-di-t-butylphenyl)-3,4,9,10-perylenedicarboximide (from Aldrich) with optimal laser excitation at 488 nm and fluorescence detection in the range 510–550 nm. At the used ~ 0.01 wt%, the dye does not affect CNLC properties. All used materials are transparent at the wavelength of 1,064 nm, so that no significant laser-induced sample heating ($> 1\,^{\circ}$C) is observed during the structure generation[28].

References

1. Woltman, S. J., Jay, D. G. & Crawford, G. P. Liquid-crystal materials find a new order in biomedical applications. *Nature Mater.* **6,** 929–938 (2007).
2. Kachynski, A. V. *et al.* Realignment-enhanced coherent anti-Stokes Raman scattering and three-dimensional imaging in anisotropic fluids. *Opt. Express* **16,** 10617–10632 (2008).
3. Camacho-Lopez, M., Finkelmann, H., Palffy-Muhoray, P. & Shelley, M. Fast liquid-crystal elastomer swims into the dark. *Nature Mater.* **3,** 307–310 (2004).
4. De Luca, A., Barna, V., Atherton, T. J., Carbone, G., Sousa, M. E. & Rosenblatt, C. Optical nanotomography of anisotropic fluids. *Nature Phys.* **4,** 869–872 (2008).
5. Clark, N. A. & Lagerwall, S. T. Submicrosecond bistable electro-optic switching in liquid crystals. *Appl. Phys. Lett.* **36,** 899–991 (1980).
6. Yang, D. K., Doane, J. W., Yaniv, Z. & Glasser, J. Cholesteric reflective display: Drive scheme and contrast. *Appl. Phys. Lett.* **64,** 1905–1907 (1994).
7. Kim, J.-H., Yoneya, M. & Yokoyama, H. Tristable nematic liquid-crystal device using micropatterned surface alignment. *Nature* **420,** 159–162 (2002).
8. van Oosten, C. L., Baastiansen, C. W. M. & Broer, D. J. Printed artificial cilia from liquid-crystal network actuators modularly driven by light. *Nature Mater.* **8,** 677–682 (2009).
9. Yamamoto, J. & Tanaka, H. Dynamic control of the photonic smectic order of membranes. *Nature Mater.* **4,** 75–80 (2005).
10. Smalyukh, I. I., Butler, J., Shrout, J. D., Parsek, M. R. & Wong, G. C. L. Elasticity-mediated nematic-like bacterial organization in model extracellular DNA matrix. *Phys. Rev. E* **78,** 030701(R) (2008).
11. Brake, J. M., Daschner, M. K., Luk, Y. Y. & Abbott, N. L. Biomolecular interactions at phospholipid-decorated surfaces of liquid crystals. *Science* **302,** 2094–2097 (2003).
12. Smalyukh, I. I., Zribi, O. V., Butler, J. C., Lavrentovich, O. D. & Wong, G. C. L. Structure and dynamics of liquid crystalline pattern formation in drying droplets of DNA. *Phys. Rev. Lett.* **96,** 177801 (2006).
13. De Gennes, P. G. & Prost, J. *The Physics of Liquid Crystals* (Oxford Univ. Press, 1995).
14. Chaikin, P. M. & Lubensky, T. C. *Principles of Condensed Matter Physics* (Cambridge Univ. Press, 2000).
15. Coles, H. J. & Pivnenko, M. N. Liquid crystal 'blue phases' with a wide temperature range. *Nature* **436,** 997–1000 (2005).
16. Clifford, M. A., Arlt, J., Courtial, J. & Dholakia, K. High-order Laguerre–Gaussian laser modes for studies of cold atoms. *Opt. Commun.* **156,** 300–306 (1998).
17. Curtis, J. E. & Grier, D. G. Structure of optical vortices. *Phys. Rev. Lett.* **90,** 133901 (2003).
18. Smalyukh, I. I. *et al.* Electric-field-induced nematic-cholesteric transition and three-dimensional director structures in homeotropic cells. *Phys. Rev. E* **72,** 061707 (2005).
19. Oswald, P., Baudry, J. & Pirkl, S. Static and dynamic properties of cholesteric fingers in electric field. *Phys. Rep.* **337,** 67–96 (2000).

20. Allen, L., Beijersbergen, M. W., Spreeuw, R. J. C. & Woerdman, J. P. Orbital angular momentum of light and the transformation of Laguerre Gaussian laser modes. *Phys. Rev. A* **45,** 8185–8189 (1992).

21. Marrucci, L., Manzo, C. & Paparo, D. Optical spin-to-orbital angular momentum conversion in inhomogeneous anisotropic media. *Phys. Rev. Lett.* **96,** 163905 (2006).

22. Brasselet, E., Murazawa, N., Misawa, H. & Juodkazis, S. Optical vortices from liquid crystal droplets. *Phys. Rev. Lett.* **103,** 103903 (2009).

23. Smalyukh, I. I., Shiyanovskii, S. V. & Lavrentovich, O. D. Three-dimensional imaging of orientational order by fluorescence confocal polarizing microscopy. *Chem. Phys. Lett.* **336,** 88–96 (2001).

24. Muhlbauer, S. *et al*. Skyrmion lattice in a chiral magnet. *Science* **323,** 915–919 (2009).

25. Dubois-Violette, E. & Pansu, B. Frustration and related topology of blue phases. *Mol. Cryst. Liq. Cryst.* **165,** 151–182 (1988).

26. Mosseri, R. Geometrical frustration and defects in condensed matter systems. *C.R. Chim.* **11,** 192–197 (2008).

27. Pansu, B., Dubois-Violette, E. & Dandoloff, R. Disclination in the S^3 blue phase. *J. Physique* **48,** 305–317 (1987).

28. Smalyukh, I. I., Kachynski, A. V., Kuzmin, A N. & Prasad, P. N. Laser trapping in anisotropic fluids and polarization controlled particle dynamics. *Proc. Natl Acad. Sci. USA* **103,** 18048–18053 (2006).

29. Gil, L. & Gilli, J. M. Surprising dynamics of some cholesteric liquid crystal patterns. *Phys. Rev. Lett.* **80,** 5742–5745 (1998).

30. Smalyukh, I. I. Confocal microscopy of director structures in strongly confined and composite systems. *Mol. Cryst. Liq. Cryst.* **477,** 23–41 (2007).

31. Nabarro, F. R. N. Singular lines and singular points of ferromagnetic spin systems and of nematic liquid crystals. *J. Physique* **33,** 1089–1098 (1972).

32. Helman, J. L. & Hesselink, L. Visualizing vector field topology in fluid flows. *IEEE Comput. Graph. Appl.* **11,** 36–46 (1991).

33. Hung, W.-C. *et al*. Surface plasmon enhanced diffraction in cholesteric liquid crystals. *Appl. Phys. Lett.* **90,** 183115 (2007).

34. Hegmann, T., Qi, H. & Marx, V. M. Nanoparticles in liquid crystals: Synthesis, self-assembly, defect formation and potential applications. *J. Inorg. Organomet. Polym. Mater.* **17,** 483–508 (2007).

35. Loudet, J. C., Barois, P. & Poulin, P. Colloidal ordering from phase separation in a liquid-crystalline continuous phase. *Nature* **407,** 611–613 (2000).

36. Poulin, P., Holger, S., Lubensky, T. C. & Weitz, D. A. Novel colloidal interactions in anisotropic fluids. *Science* **275,** 1770–1773 (1997).

37. Smalyukh, I. I., Lavrentovich, O. D., Kuzmin, A. N., Kachynskii, A. V. & Prasad, P. N. Elasticity-mediated self-organization and colloidal interactions of solid spheres. *Phys. Rev. Lett.* **95,** 157801 (2005).

38. Stebe, K. J., Lewandowski, E. & Ghosh, M. Oriented assembly of metamaterials. *Science* **325,** 159–160 (2009).

39. Kang, S.-W. & Chien, L.-C. Field-induced and polymer-stabilized two-dimensional cholesteric liquid crystal gratings. *Appl. Phys. Lett.* **90,** 221110 (2007).

40. Lu, S.-Y. & Chien, L.-C. A polymer stabilized single-layer color cholesteric liquid crystal display with anisotropic reflection. *Appl. Phys. Lett.* **91,** 131119 (2007).

41. Leach, J., Dennis, M. R., Courtial, J. & Padgett, M. J. Vortex knots in light. *New J. Phys.* **7,** 1–11 (2005).

42. Leach, J., Dennis, M. R., Courtial, J. & Padgett, M. J. Laser beams: Knotted threads of darkness. *Nature* **432,** 165 (2004).

43. Irvine, W. T. M. & Bouwmeester, D. Linked and knotted beams of light. *Nature Phys.* **4,** 716–720 (2008).

44. Anderson, V. J. & Lekkerkerker, H. N. Insights into phase transition kinetics from colloid science. *Nature* **416,** 811–815 (2002).

45. Hud, N. V., Downing, K. H. & Balhord, R. A constant radius of curvature model for the organization of DNA in toroidal condensates. *Proc. Natl Acad. Sci. USA* **92,** 3581–3585 (1995).

46. Kulic, I. M., Andrienko, D. & Deserno, M. Twist-bend instability for toroidal DNA condensates. *Europhys. Lett.* **67,** 418–424 (2004).

47. Livolant, F. & Bouligand, Y. Double helical arrangement of spread dinoflagellate chromosomes. *Chromosoma* **80,** 97–118 (1980).

48. Grier, D. G. A revolution in optical manipulation. *Nature* **424,** 810–816 (2003).

Acknowledgements

Author contributions

I.I.S. and R.P.T. carried out all experimental work. I.I.S. was responsible for project planning and tentative explanation. Y.L. did computer simulations of structure and elasticity and I.I.S. simulated the intensity distribution. I.I.S., Y.L., N.A.C. and R.P.T. were responsible for writing the article. All authors discussed the results and commented on the manuscript.

Additional information

The authors declare no competing financial interests. Supplementary information accompanies this paper on www.nature.com/naturematerials. Reprints and permissions information is available online at http://npg.nature.com/reprintsandpermissions. Correspondence and requests for materials should be addressed to I.I.S.

Three-dimensional structure and multistable optical switching of triple twisted particle-like excitations in anisotropic fluids

[1,2,3,*]Ivan I. Smalyukh, [2,4]Yves Lansac, [1,2]Noel A. Clark, and [1,2]Rahul P. Trivedi

1. Free energy and director structure

We use numerical minimization of free energy to obtain the static equilibrium and metastable configurations of $\hat{n}(\vec{r})$ in confined CNLCs. The spatio-temporal evolution of the T3 structures being generated by LG beams and during the unwinding transition under the action of an external electric field has been explored using computer simulations too and will be discussed in details elsewhere. The free energy density for a CNLC of pitch p under an external electric field $\vec{E}_{LG}$ of the LG beam is given by $f_{total} = f_{elastic} + f_{field}$, where

$$f_{elastic} = \frac{K_{11}}{2}(\nabla \cdot \hat{n})^2 + \frac{K_{22}}{2}[\hat{n} \cdot (\nabla \times \hat{n}) \pm \frac{2\pi}{p}]^2 + \frac{K_{33}}{2}[\hat{n} \times (\nabla \times \hat{n})]^2 - K_{24}[\nabla \cdot [\hat{n}(\nabla \cdot \hat{n}) + \hat{n} \times (\nabla \times \hat{n})]]$$

$$f_{field} = -\frac{\varepsilon_0 \Delta \varepsilon}{2}(\vec{E}_{LG} \cdot \hat{n})^2$$

[1]*Department of Physics, University of Colorado, Boulder, Colorado 80309, USA. *e-mail: ivan.smalyukh@colorado.edu*

[2]*Liquid Crystal Materials Research Center, University of Colorado, Boulder, Colorado 80309, USA.*

[3]*Renewable and Sustainable Energy Institute, University of Colorado, Boulder, Colorado 80309, USA.*

[4]*Laboratoire d'Electrodynamique des Matériaux Avancés, Université François Rabelais-CNRS-CEA, UMR 6157, 37200 Tours, France*

The K_{24}-term describes the saddle-splay elastic deformations and is known to play a key role in stabilizing the blue phases (BPs) formed by a 3-dimensional crystalline organization of double-twist cylinders.[13] The saddle-splay constant K_{24} is difficult to measure experimentally but it is reasonable to assume that $K_{24} = K_{22}$.[49,50] $\Delta \varepsilon = n_e^2 - n_o^2$ is the dielectric anisotropy of the CNLC at the used laser frequency such that $\hat{n}(\vec{r})$ aligns parallel ($\Delta \varepsilon > 0$) to $\vec{E}_{LG}$.

The minimization of the free energy to find the equilibrium director field is performed using a relaxation method.[29] Equilibrium 3D-structures of $\hat{n}(\vec{r})$ have $\delta F / \delta n_i = 0$, where n_i is the projection of the director $\hat{n}(\vec{r})$ onto the i-axis (i = 1(x), 2(y), 3(z)) and $\delta F / \delta n_i$ are the functional derivatives of the Frank free energy defined as $F = \int f_{total} dV$ with V being the volume of the sample. From a numerical point of view, the spatial derivatives of the director are computed using a 4th order finite difference scheme. Periodic boundary conditions are applied along $\hat{x}$- and $\hat{y}$- directions while fixed homeotropic boundary condition are used along $\hat{z}$-direction. At each step Δt, the functional derivatives $\delta F / \delta n_i$ are computed and the resulting elementary displacement δn_i defined as $\delta n_i = -\Delta t \dfrac{\delta F}{\delta n_i}$ is projected onto the surfaces $n^2 = 1$ and is taken into account only if it leads to a decrease in the Frank free energy F. Otherwise, the increment Δt is decreased. This procedure is repeated until the elementary displacement is smaller than a given value set to 10^{-8}. The discretisation is done on fairly large grids (N_x x N_y x N_z) with $N_x = N_y = 119$ and $N_z = 35$, or $N_x = N_y = 239$ and $N_z = 71$ in order to make sure that the minimum-energy $\hat{n}(\vec{r})$ is indeed a structure localized in space in equilibrium with the surrounding untwisted CNLC and that the periodic boundary conditions do not introduce artifacts affecting its stability. Using grid spacing such as $h_x = h_y = h_z = 0.05$ μm and $N_z = 71$ gives sample thickness d = 3.50 μm. All presented simulations have been done for material parameters of nematic host ZLI-3412 provided in the Table 1.

Two different types of initial conditions were tested as a starting point of the minimization procedure described above, both leading to the equilibrium Toron structures. The first type corresponds to a director field configuration close to the one deduced from the FCPM experiments (Figs. 1, 3, and Supplementary Figs. S1-S3). The second type is obtained by using

electric fields of Laguerre-Gaussian beams that have torus-like intensity distributions (Fig. 1g-j) and that induce toroid-shaped initial deformations of the director field depending on the charge l and radius R of the vortex beam in its lateral plane. In agreement with experiments, the initial location of the beam's focal plane across the sample's thickness does not have a significant effect on the spatial location of the generated Toron. Although most of the numerical results that we present in this work have been obtained for $d/p = 1$, we were able to stabilize T3-like structures for a range of values $d/p = 0.75 - 1.3$, and find them being minimum-energy structures for *d/p*=0.9-1.3 (Supplementary Fig. S4a). The Torons are well-defined localized structures for $d/p \leq 1$ with their reduced lateral size L/p comparable to d/p (Supplementary Fig. S4b), where L is the diameter of the twist-escaped λ-disclination ring. For $d/p > 1$, the Torons have an extended disclination ring and their reduced lateral size *>d/p* (Supplementary Fig. S4b). The relative energy of a 2D-hexagonal lattice of T3-1s, 2D linear arrays of cholesteric fingers of the first and second kinds (CF1 and CF2, respectively),[18,19] as well as translationally invariant cholesteric (TIC) and untwisted nematic (Nem) configurations[18] are compared in Fig. S4a (as computed for the volume of a unit cell of the hexagonal lattice formed by Torons of the largest observed L/p). These results show that T3-1 can be stabilized within a broad range of d/p=0.75-1.3, corresponding to either the global or local free energy minimum.

2. Topological Skeleton.

The critical points and the topological skeleton are computed by formerly rewriting the director field as a set of ordinary differential equations (ODEs): $d\vec{x}/dt = \hat{n}(x,y,z)$, with t being an arbitrary parameter (not the time). This approach connects the dynamical system theory and the director field and allows applying qualitative theory of differential equations in the "physical space" rather than the phase plane of solutions of a system of ODEs. Similar approaches are extensively used, for example, in the field of computational fluid dynamics.[31,32,51,52] Stationary points $\vec{x}_c(x_c, y_c, z_c)$ are such that $\hat{n}(\vec{x}_c) = \vec{0}$. We can further investigate the structure of the trajectories close to the stationary point by examining the Jacobian matrix of the partial derivatives of the director field, $J\hat{n} = \partial n_i / \partial x_j$ with $(x_j \equiv x, y, z)$. If

this matrix is non-singular, the stationary point $\vec{x}_c(x_c, y_c, z_c)$ is a critical point.[51] The eigenvalues and eigenvectors of the Jacobian describe the local behavior around a critical point. We have used the numerical library *pfskel*[53] to find the positions of the critical points C_1 and C_2, located near the top and the bottom glass plates, respectively. Both C_1 and C_2 have one real eigenvalue and two complex conjugate eigenvalues. The two eigenvectors corresponding to the complex eigenvalues define a plane roughly parallel to the glass plates while the direction associated to the real eigenvalue is roughly along the $\hat{z}$-axis. The critical points are hyperbolic and the fact that we have two complex conjugate eigenvalues indicates that the director field spirals around these defects.[51] We have computed the streamlets (flow lines representing the motion of a massless particle) tangent to the director field. The streamlets originate very close from the critical point (defect) locations and move along the eigendirections of C_1 and C_2. Equations of motion are solved using either a 2nd or a 4th order Runge-Kutta forward or backward (depending whether we are moving along a repulsive or an attractive direction) integrator. These calculations have been performed using *pfskel* and OpenDX (the open source version of IBM's Data Explorer has been used for visualizations presented in this work). The two isolated critical points with the streamlets as well as the twist-escaped disclination ring (axis of the torus) define the topological skeleton of the Toron structure shown in Fig. 4f.

The detailed description of computer simulations (using both vectorial and tensorial approaches for minimization of elastic free energy[54-56]) compared to the experimental study of director field configurations as well as topological analysis for the experimentally-observed T3-2s and T3-3s will be reported elsewhere.

SUPPLEMENTARY REFERENCES

Numbering continues from the reference list in the main text of the manuscript.

49. Allender, D.W., Crawford, G.P., and Doane, J. W. Determination of the liquid-crystal surface elastic constant K_{24}. *Phys. Rev. Lett.* **67**, 1442-1445 (1991).

50. Polak, R.D., Crawford, G.P., Costival, B.C., Doane, J.W. and Zumer, S. Optical determination of the saddle-splay elastic constant K_{24} in nematic liquid crystals. *Phys. Rev. E* **49**, R978 (1994).

51. Asimov, D. Notes on the topology of vector fields and flows. *Tech. Rep., NASA Ames Research Center*. RNR-93-003 (1993).

52. Globus, A., Levit, C. and Lasinski, T. A tool for visualizing the topology of three-dimensional vector fields. *Proc. IEEE Visualization '91, IEEE Computer Society Press*, 33-40 (1991).

53. Cornea, N.D., Silver, D., Yuan, X. and Balasubramanian, R. Computing hierarchical curve-skeletons of 3D objects. *The Visual Computer* **21**, 945-955 (2005).

54. Anderson, J. E., Watson, P. E. & Bos, P. J. LC3D: Liquid crystal display 3-D director simulator software and technology guide (Artech House, Boston, 2001)

55. Gil., L. J. Numerical resolution of the cholesteric unwinding transition problem. *J. Phys. II France* **5,** 1819-1833 (1995)

56. Sonnet, A. Kilian, A. & Hess, S. Alignment tensor versus director: Description of defects in nematic liquid crystals. *Phys. Rev. E* **52,** 718-722 (1995)
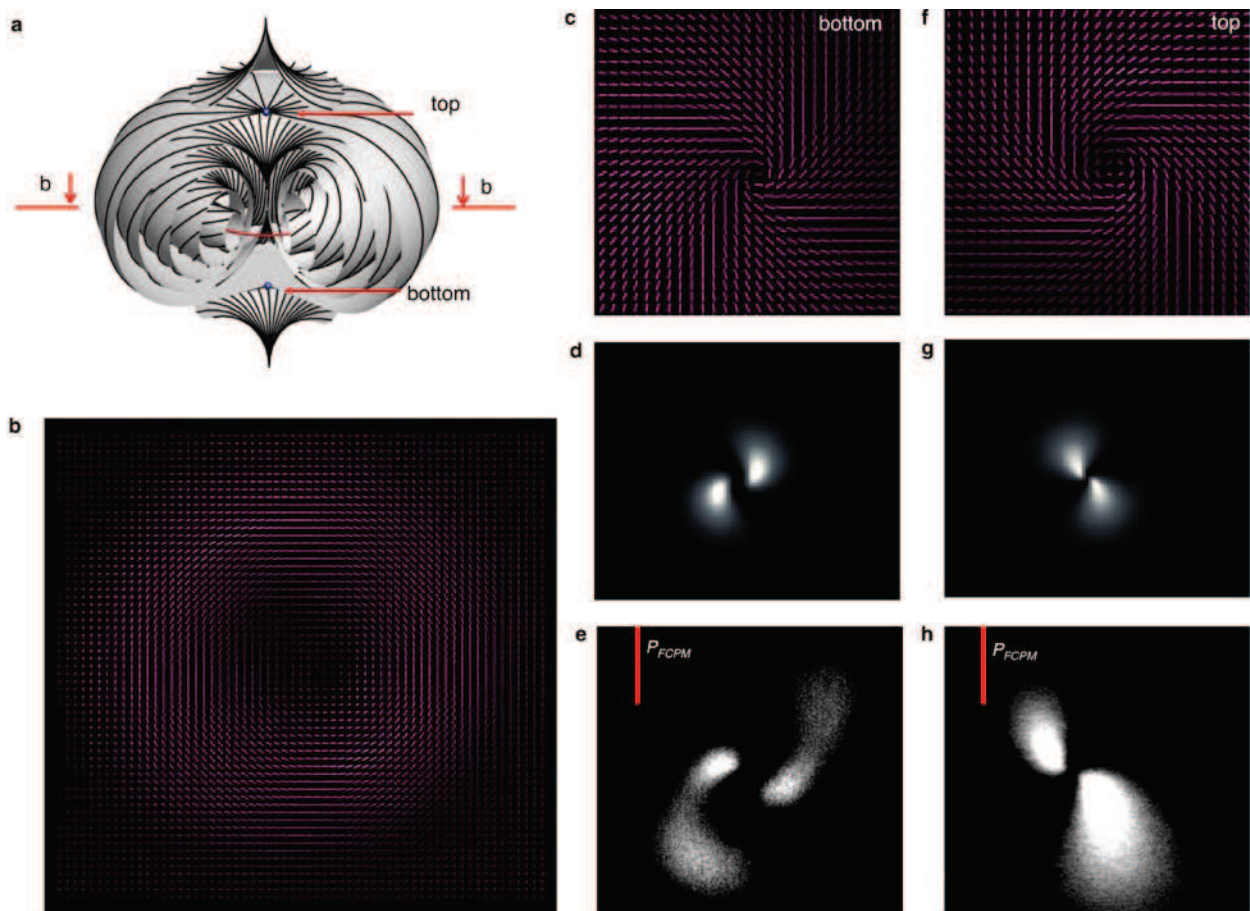
SUPPLEMENTARY FIGURES

Figure S1. Computer simulations and FCPM imaging of the in-plane cross-sections of the T3-1 structure. a, Schematic representation of the cell with the hyperbolic point defects shown by blue dots and the twist escaped non-singular disclination ring shown by a red line. **b,** Computer simulated $\hat{n}(\vec{r})$ in the central plane (b-b cross-section shown in **a**) of the T3-1 structure coplanar with the disclination ring. **c,f,** In-plane cross-sections of $\hat{n}(\vec{r})$ in the vicinity of point defects near the bottom plate, **c,** and the top plate, **f. d,g,** Corresponding simulated and **e,h,** experimental FCPM textures. The red bars in **e** and **h** indicate the corresponding FCPM linear polarization states.
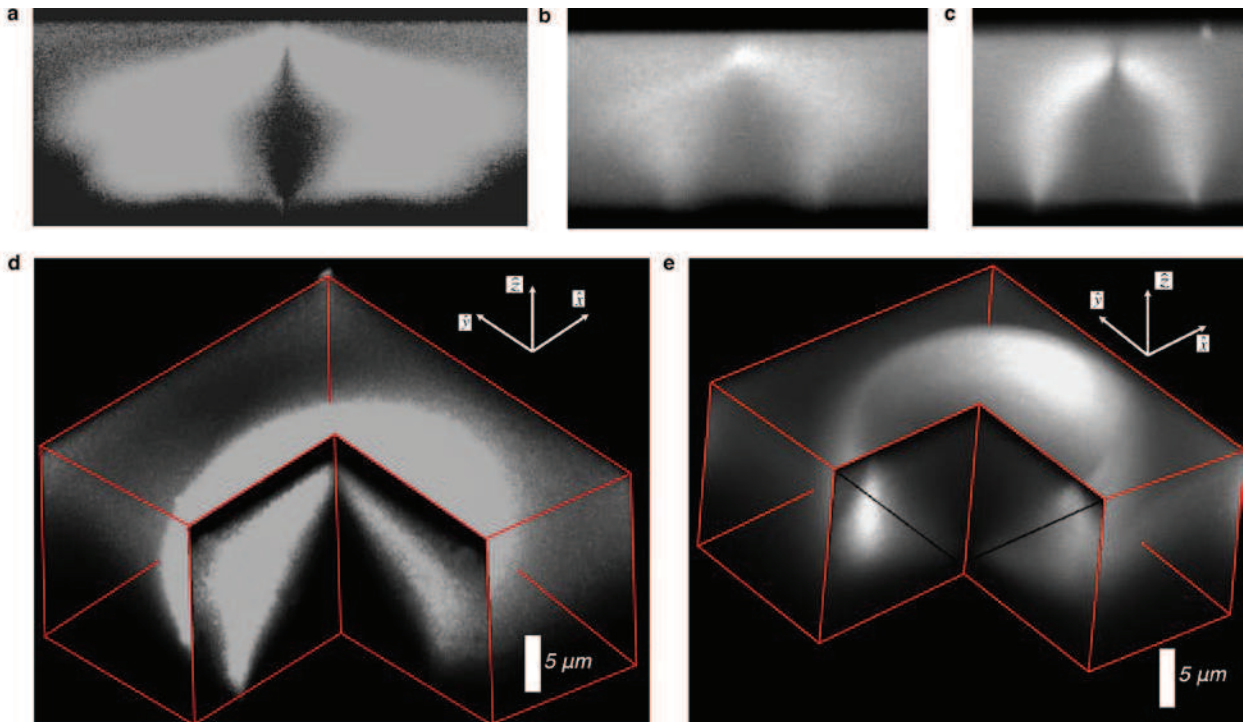
Figure S2. FCPM imaging of the T3-2s with different locations and diameters of disclination rings. a-c, FCPM vertical cross-sections of three different T3-2s in a cell of thickness $d = 15\mu m$ with different diameters of the disclination ring at the bottom surface. **d,e**, 3D FCPM images of the T3-2 structures having the disclination rings **d** at the bottom and **e** at the top surface.
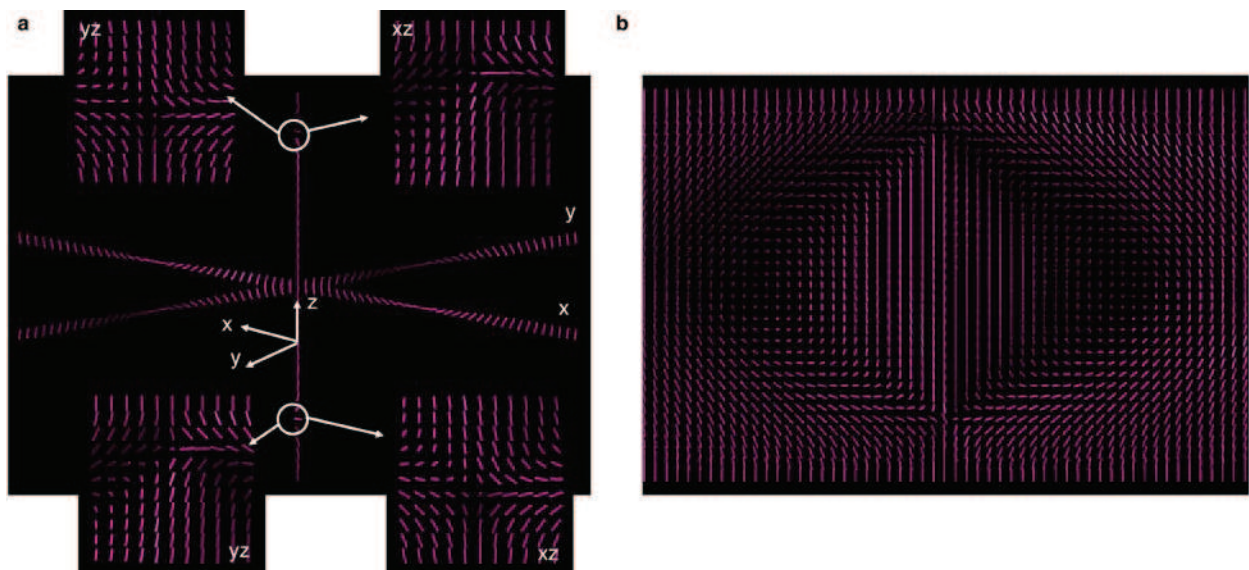
Figure S3. Computer-simulated vertical cross-sections of the T3-1 structure. a, The structure consists of the radial twist of $\hat{n}(\vec{r})$ in the central plane of the cell as well as two point defects close to the substrates; the insets show simulated $\hat{n}(\vec{r})$ in mutually-orthogonal xz and yz cross-sections intersecting the hyperbolic point defects at the top and bottom glass plates. **b,** Computer-simulated director field in the axial cross-section.
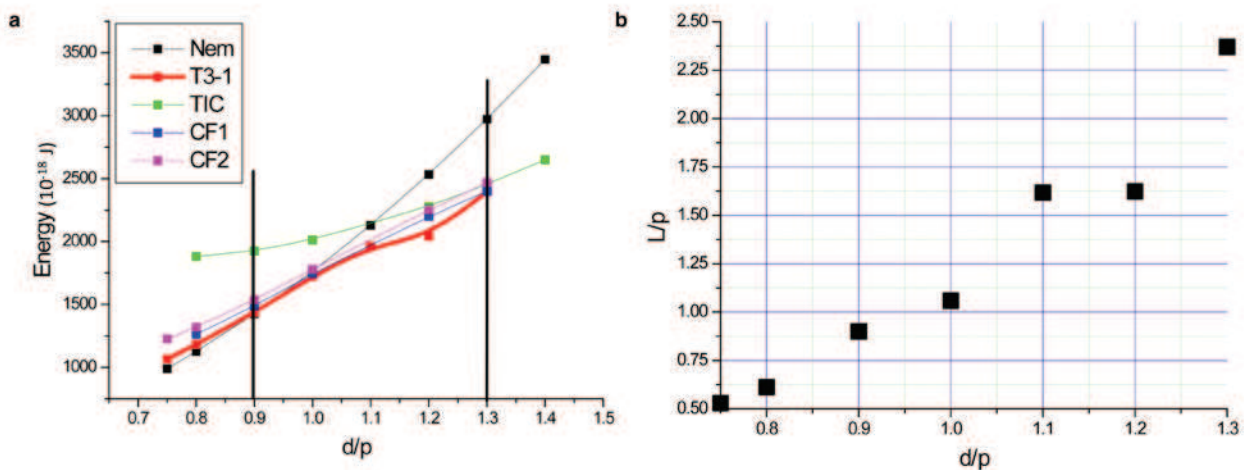
Figure S4. Elastic free energy and the reduced diameter of the T3-1 configuration as a function of *d/p*. a, Free energy of a hexagonal array of T3-1s computed for a unit cell volume of $\approx 38 \mu m^3$ as compared to that of an equivalent sample volume with the twisted invariant configuration (TIC)[18,19], untwisted nematic-like structure (Nem) and linear arrays of two different cholesteric fingers CF1 and CF2[18,19] (the density is calculated for the volume of the unit cell of a 2D hexagonal lattice formed by Torons). **b,** Normalized equilibrium diameter L/p of the T3-1 structure as a function of d/p.